

1 **Soil Moisture Memory in Commonly-used Land Surface Models Differ Significantly**
2 **from SMAP Observation**

3 **Qing He¹, Hui Lu^{1,2} and Kun Yang¹**

4 ¹Ministry of Education Key Laboratory for Earth System Modeling and the Department of Earth
5 System Science, Tsinghua University, Beijing, 100084, China

6 ²Ministry of Education Ecological Field Station for East Asian Migratory Birds, Beijing, 100084,
7 China

8 Corresponding author: Hui Lu (luhui@tsinghua.edu.cn)

9
10
11
12
13 **Key Points:**

- 14 • The four prevailing LSMs show similar misestimation of soil moisture memory
15 compared to SMAP observation.
- 16 • The differences between LSMs and SMAP are highly dependent on the models'
17 parameterizations.
- 18 • The soil parameters may play an essential role in determining the LSMs' L-A coupling
19 biases.

20
21
22

23 **Abstract**

24 Weather and climate forecast predictability relies on Land-Atmosphere (L-A) interactions
25 occurring at different time scales. However, evaluation of L-A coupling parameterizations in
26 current land surface models (LSMs) is challenging since the physical processes are complex, and
27 large-scale observations are scarce and uncommon. Recent advancements in satellite observations,
28 in this light, provide a unique opportunity to evaluate the models' performances at large spatial
29 scales. Using 5-year soil moisture memory (SMM) from Soil Moisture Active and Passive (SMAP)
30 observations, we evaluate L-A coupling performances in 4 prevailing LSMs with both coupled
31 and offline simulations. Multi-model mean comparison at the global scale shows that current
32 LSMs tend to overestimate SMM that is controlled by water-limited processes and vice versa.
33 Large model spreads in SMM are also observed between individual models. The SMM biases are
34 highly dependent on models' parameterizations, while showing minor relevance to the models'
35 soil layer depths or the models' online/offline simulating schemes. Further analyses of two
36 important terrestrial water cycle-related variables indicate current LSMs may underestimate soil
37 moisture that is directly available for evapotranspiration and global flood risks. Finally, a
38 comparison of two soil moisture thresholds indicates that the soil parameters employed in LSMs
39 play an essential role in producing the model's biases. The satellite estimation of ET at the water-
40 limited stage and soil hydraulic parameters provides readily available information to constrain
41 LSMs, which are essentially important to improve the models' L-A coupling simulations, as well
42 as other land surface processes such as terrestrial hydrological cycles.

43

44 **Plain Language Summary**

45 To have a more accurate weather forecast, a better description of physical processes between Land
46 and Atmosphere (L-A) is required. The L-A processes are often characterized by Land Surface
47 Models (LSMs). However, because such processes are complex, and the observation records are
48 scarce, it is difficult to evaluate the L-A simulations in current LSMs on large scale. Recent
49 advances in satellite technology provide a unique opportunity to evaluate the LSMs' performances
50 on basis of observed evidence.

51 In this study, we use SMAP-observed SMM to evaluate the four most widely-used LSMs. Results
52 show that the four LSMs tend to overestimate SMM that is controlled by the water-limited
53 processes and vice versa. Large differences between models are observed, showing high
54 dependence on the model's parameterizations. Two water cycle-related variables are also
55 analyzed, indicating the LSMs may underestimate soil moisture that is directly available for
56 evapotranspiration and global flood risks. Finally, a comparison of the models' soil parameters
57 shows that these parameters play an essential role in producing the models' biases. This study
58 provides a comprehensive evaluation of L-A simulating performances in several prevailing LSMs.
59 This study also provides useful information to constrain LSMs, which are important to improve
60 Earth's land surface simulations.

61

62 **1 Introduction**

63 Land-atmosphere (L-A) interactions occurring at different timescales are important for
64 regional weather and climate (Seneviratne et al., 2010). For example, the coupling of surface water
65 and temperature anomalies can intensify the evolutions of extreme events such as droughts and

66 heatwaves (Koster et al., 2009; Miralles et al., 2019, 2014; Seneviratne et al., 2006). However, the
67 L-A coupling processes are complex and often interact with each other. As such, current climate
68 models often present large model uncertainties in characterizing L-A coupling strength, for
69 example, previous studies have shown that there are large differences between soil moisture (SM)
70 and precipitation coupling strength in several prevalently-used global climate models (Guo et al.,
71 2006; Koster et al., 2006, 2002). Similar model spreads are also found in coupling strength between
72 SM and evapotranspiration (ET)(Berg and Sheffield, 2018; Dirmeyer et al., 2006). However, since
73 large-scale observations of essential L-A variables (e.g., SM and ET) are scarce (Pastorello et al.,
74 2020; Seneviratne et al., 2010), recent assessments are limited to inter-model comparisons only.
75 However, in order to improve the models' L-A coupling performance, it is essentially important
76 to diagnose individual models' biases with observational evidence. In this light, recent advances
77 in satellite technologies provide unique opportunities to investigate L-A coupling processes at
78 large spatial scales.

79 A diversity of methods have been developed to characterize L-A coupling strength, where
80 algorithms based on sensitivity analyses, e.g., correlation and covariance analyses (Dirmeyer,
81 2011; Dirmeyer et al., 2009; Miralles et al., 2014), and partial differentiation between multiple L-
82 A variables (Feldman et al., 2019; Gallego-Elvira et al., 2016; Schwingshackl et al., 2017), are
83 favored since they present explicit physical indications to understand. However, since the
84 sensitivity analyses require at least two L-A variables, it is even more challenging to obtain
85 observational records at large spatial scales. By contrast, soil moisture memory (SMM) – an L-A
86 coupling metric that is based solely on SM time series – could facilitate L-A coupling assessment
87 studies for less dependence on data availability, especially when a large number of models are
88 analyzed (e.g., common variables should be selected when using multi-variable analyses, which
89 may reduce the model numbers; using SMM instead can efficiently avoid this problem).

90 SMM measures the time when soil moisture recovers to equilibrium from perturbations (a
91 perturbation can refer to either a wet anomaly such as precipitation or a dry anomaly such as
92 drought). Methods such as e-folding time based on the Markov process (Delworth and Manabe,
93 1988; Koster and Suarez, 2001) and time scale based on soil moisture integral (Ghannam et al.,
94 2016; Katul et al., 2007) are developed to quantify SMM. In these studies, shorter SMM time
95 indicates more rapid water and energy exchanges between land and near-surface atmosphere –
96 thus stronger L-A coupling strength. However, while the methods based on Markov processes
97 provide overall L-A coupling indications, they do not characterize land processes occurring at
98 different time scales (e.g., drainage occurring within hours or days and ET processes occurring at
99 subweekly to weekly after precipitation events). In other words, SMM based on Markov processes
100 does not provide explicit physical indications for calibrating models' parameterizations. A recently
101 developed hybrid model does so by separating the effects of water- and energy-limitations on
102 surface processes (McColl et al., 2019). By comparing the satellite estimates with one example
103 land surface model (LSM), the study demonstrates that the LSM tends to overestimate SMM time
104 at long-term scales whereas underestimates SMM at short-term time scales.

105 However, it is still unknown whether the above conclusion is a common nature in most
106 LSMs – the L-A coupling parameterization schemes in LSMs are usually highly model-dependent,
107 and can be susceptible to individual models' configurations, e.g., soil layer depth, online/offline
108 simulating schemes, critical L-A parameters, etc. Moreover, in McColl et al. (2019) the satellite-
109 based SMM are estimated from single-year soil moisture time series due to limitations in data
110 availability. However, the annual variability of soil moisture could influence the conclusions. In

111 this light, multi-model assessments of L-A coupling characteristics at different time scales are
112 necessary to diagnose biases and further provide a reference to improve L-A coupling simulations
113 in current LSMs.

114 In this study, we provide a comprehensive evaluation of L-A coupling characteristics in
115 several prevalently-used LSMs (i.e., Noah LSM, Catchment LSM, HTESSSEL and SiB) by using
116 SMM estimated from 5-year satellite observations. We intend to address the two following
117 questions: (1) Compared to large-scale satellite observations, how do the prevailing LSMs perform
118 in simulating L-A coupling characteristics? (2) Despite the models' spreads, do the LSMs show
119 common characteristics in L-A simulations and what might be the essential factors that contribute
120 to them? To answer these questions, spatial patterns and annual variability of SMM from satellite
121 estimations are first analyzed to provide a robust reference for multi-model assessments. Multi-
122 model performances and influences of individual model's configurations including soil layer
123 depths and coupling schemes are then evaluated. In order to diagnose possible reasons that may
124 result in the models' biases, satellite-observed terrestrial water cycle parameters (i.e., precipitation
125 stored in surface soil layer and ET at the water-limited stage) and soil moisture thresholds (i.e.,
126 soil wilting point θ_w and soil critical point θ_*) indicated from soil moisture memory are extracted
127 and further compared with LSMs. The analyses provide satellite-based reference to diagnose L-A
128 coupling characteristics in several prevailing LSMs, and provide readily available datasets to
129 constrain the models' simulations at the global scale.

130

131 **2 Materials and Methods**

132 In this section, we will first give a brief review of basic concepts relevant to SMM. Explicit
133 equations of the analyzed variables in this study are then given to address their physical indications.

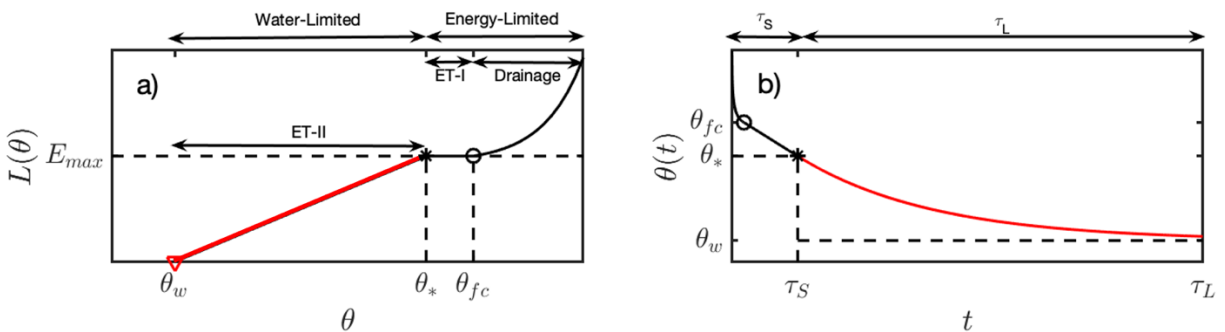
134 SMM refers to the time between a perturbation starts and ceases in the time domain. Taking
135 the wet scenario for example, when a perturbation occurs soil moisture loses water to the near-
136 surface atmosphere through flux exchanges. The water loss persists with several sub-processes in
137 order: (i) Drainage and runoff start to happen immediately after the precipitation when soil
138 moisture is saturated; the two subprocesses cease when soil moisture is below the level when soil
139 capillary is not able to hold water (field capacity, θ_{fc}); (ii) when soil moisture is below θ_{fc} , but is
140 above a certain level (typically defined as the critical point, θ_c), the soil starts to evaporate at the
141 maximum ET rate (also called Stage-I ET); (iii) When soil moisture is below θ_c , ET starts to
142 happen at the water-limited rate (also named as Stage-II ET; the water-limited ET rate is typically
143 determined by soil moisture content by first-order); (iv) the soil ceases to lose water when soil
144 moisture is below soil wilting point θ_w . The entire loss can be defined as a function of soil
145 moisture, i.e., Loss Function. The loss function can then be divided into two broad categories.
146 When soil moisture is wet (i.e., above θ_c), the function is controlled by energy terms; otherwise,
147 the function is limited by water conditions. The above processes can be described in Figure 1.

148 The energy-limited processes (i.e., drainage and stage-I ET) generally occur on timescales
149 of hours to days. To identify these processes, soil moisture datasets with the comparable temporal
150 resolution are required. Traditional SMM methods based on Markov processes (or other red-noise
151 processes) were mostly developed based on soil moisture data with rather coarse temporal
152 resolutions (e.g., monthly) due to data limitations. They generally combine the above physical

153 processes at different stages. Therefore, the derived SMM only represents the overall L-A coupling
 154 strength without explicit physical indication. This impedes LSMs development since such L-A
 155 strength cannot be readily used for models' calibration.

156 The recently developed method based on a hybrid model instead characterizes SMM by
 157 considering energy- and water-limitations separately. The hybrid model is developed by using
 158 satellite soil moisture data with a temporal resolution of 3 days. Compared to traditional SMM
 159 results, the SMM at the energy- and water-limited stage can provide detailed references for
 160 calibration in LSMs, e.g., diagnosing which specific processes the L-A coupling biases come from.
 161 The hybrid model separates Loss Function by surface water conditions (i.e., the occurrence of
 162 precipitation events), and explicit equations for SMM at different regimes as well as relevant
 163 diagnoses are given in the following context.

164



165

166 Figure 1 Schematic of surface water loss process (a) and soil moisture memory at
 167 different loss regimes (b). Figures are adapted from McColl et al. (2017b). Note that the *x-axis*
 168 in (a) refers to soil moisture ($\text{m}^3 \text{m}^{-3}$), and *y-axis* refers to surface water loss rate ($L(\theta)$, e.g.,
 169 mm s^{-1}); E_{max} is the maximum evapotranspiration rate (the same unit as $L(\theta)$). While in (b), *x-*
 170 *axis* refers to time (e.g., days) and *y-axis* refers to soil moisture content ($\text{m}^3 \text{m}^{-3}$). θ_w , θ_* , and θ_{fc}
 171 refers to soil wilting point, critical point, and field capacity, respectively.

172 2.1 Soil moisture memory time at water-limited regime (τ_L) and energy-limited regime (τ_S)

173 Soil moisture memory in the water-limited regime (τ_L , L for the water-limited processes
 174 that usually occur at long time scales) and energy-limited regime (τ_S , S for the water-limited
 175 processes that usually occur at short time scales) are estimated from the hybrid model following
 176 McColl et al. (2019). The water-limited regime (i.e., Stage-II ET) is characterized by a
 177 deterministic equation since the processes at this stage usually occur in multi-days, a time scale
 178 that modern satellite measurements can characteristically resolve. Correspondingly, the water
 179 losses during the energy-limited stage often occur much more rapidly (e.g., hours to half a day).

180 In this case, a stochastic model is developed to describe a combination of unresolved processes
 181 (e.g., drainage, runoff and Stage-I ET). The hybrid model can be written as:

$$182 \quad \frac{d\theta(t)}{dt} = \begin{cases} -\frac{\theta(t)-\theta_w}{\tau_L}, & P = 0 \\ -\frac{\theta(t)-\bar{\theta}}{\tau_S} + \varepsilon(t), & P > 0 \end{cases} \quad (1)$$

183 where, P refers to precipitation occurrence (a binary variable); θ is the volumetric soil moisture,
 184 and $\bar{\theta}$ refers to the time average soil moisture; ε is an independent random variable with a mean
 185 of zero; τ_L and τ_S refers to the soil moisture memory at the water-limited stage and energy-limited
 186 stage, respectively. Solving the above equations yields the explicit expressions of τ_L and τ_S , as:

$$187 \quad \theta(t) = \begin{cases} \Delta\theta \exp\left(-\frac{t-\Delta t_p}{\tau_L}\right) + \theta_w, & P = 0 \\ \overline{\theta(t - \Delta t_p)} + \frac{\alpha}{\Delta z} \exp\left(-\frac{\Delta t_p}{2\tau_S}\right), & P > 0 \end{cases} \quad (2a)$$

$$(2b)$$

188 where, $\Delta\theta$ refers to the soil moisture change during each soil drying event; θ_w refers to the
 189 minimum soil moisture value; α is the precipitation intensity; Δz is the depth of surface soil layer,
 190 and $t = \Delta t_p$ refers to the time when the soil moisture drying starts to occur.

191 The energy-limited memory τ_S can then be calculated directly by rearranging the
 192 expression in (2b), as:

$$193 \quad \tau_S = -\frac{\frac{\Delta t}{2}}{\log\left(\frac{\Delta z \overline{\theta_+}}{\alpha}\right)} \quad (3)$$

194 where $\overline{\theta_+} = \theta(t) - \overline{\theta(t - \Delta t)}$ refers to the positive increments of soil moisture; Δt refers to the
 195 temporal resolution of the input data.

196 However, since soil moisture is the only observation in (2a), and there are multiple
 197 unknowns (i.e., τ_L and θ_w) to be parametrized, τ_L is then estimated by fitting the function to the
 198 soil moisture samples that are subject to water-limitation, namely, the drydown events. Drydown
 199 events here are identified as an event when the soil moisture changes are consistently negative.
 200 Additional rules including (1) θ_w is limited to be lower than the minimum value of the soil moisture
 201 time series; and (2) drydown events with less than 3 observation samples and events with $R^2 <$
 202 0.7 are filtered are applied to ensure credible fitting performance, consistent to McColl et al.
 203 (2017).

204 **2.2 Terrestrial water cycle diagnostics informed from SMM**

205 In addition to informing L-A coupling strength, another important role of soil memory is
 206 to provide relevant diagnostics of terrestrial water cycles. Specifically, the stored precipitation
 207 fraction F_p in τ_S provides an explicit estimation of how much precipitation can be retained by the
 208 surface soil layer. Therefore, it reflects the water-holding capacity of the soil. A decrease of F_p
 209 indicates the loss of soil water-holding capacity – thus more water will be stored in the near-surface
 210 atmosphere and induce the positive anomaly of rainfall and surface runoff (Liu et al., 2021). In

211 this light, F_p can be viewed as a reasonable proxy for assessing flood risks in terrestrial water
 212 cycles. F_p can be described as the sum of positive soil moisture increments normalized by the total
 213 precipitation during a contemporary period and calculated as:

$$214 \quad F_P(f) = \frac{\Delta z \sum_{i=1}^{fT} \Delta \theta_{i+}}{\int_0^T P(t) dt}, \quad (4)$$

215 where, f refers to the sampling frequency of the input data (d^{-1}) and T refers to the analyzed time
 216 period (days); Δz refers to soil layer depth (mm), $\Delta \theta_{i+}$ refers to positive soil moisture increments
 217 ($\text{m}^3 \text{m}^{-3}$); $\int_0^T P(t) dt$ is the accumulated precipitation (mm).

218 By using one-year SMAP soil moisture retrieval, McColl et al. (2017) has demonstrated a
 219 global median estimation of 0.14, that is, a thin 50mm soil layer (SMAP's nominal detecting depth)
 220 can retain approximately 14% of the precipitation falling on land. Subsequent studies have since
 221 referred to this amount as a benchmark to evaluate F_p in varying soil and climate conditions or
 222 how F_p will change in the future climate (Kim and Lakshmi, 2019; Liu et al., 2021; Martínez-
 223 Fernández et al., 2020). However, since soil moisture and precipitation both show annual
 224 variabilities, and the original SMAP products can contain larger noises compared to recent SMAP
 225 versions using an improved algorithm (e.g., Dual Channel Algorithm, MTDCA), it is necessary to
 226 examine the robustness of F_p distribution originally reported in McColl et al. (2017).

227 In terrestrial water cycles, ET is a core but difficult-to-estimate variable. Initially, gridded
 228 ET products have been developed to validate and improve simulations of soil moisture and other
 229 water-related variables in LSMs. At this phase, diverse ET products based on satellite estimations
 230 (Hu and Jia, 2015; Mu et al., 2014, 2007) and biophysical-constrained model datasets (Zhang et
 231 al., 2019; Zhao et al., 2019) have been developed, while most of them have shown moderate data
 232 accuracy compared to in-situ observations. However, few current ET products provide the ET
 233 information limited by surface water and energy availability, which plays an increasingly
 234 important role in the latest generation of LSMs. However, by integrating the surface water loss in
 235 the water-limited soil drying stage, the Stage-II ET can be readily estimated in this study to
 236 calibrate models' representations of surface water and energy variables. Annual accumulated
 237 Stage-II ET is calculated as:

$$238 \quad ET_{II} = \sum_{i=1}^n \Delta z \theta_* (1 - \exp(-\frac{\Delta d d_i}{\tau_L})), \quad (5)$$

239 where, Δz is the soil layer depth (mm); θ_* refers to soil critical point ($\text{m}^3 \text{m}^{-3}$), $\Delta d d_i$ refers to
 240 duration each drydown event persists (days), where n refers to the total soil moisture drydown
 241 number within the analyzed year, and i refers to the drydown event; τ_L indicates water-limited
 242 SMM (days).

243 2.3 Critical Soil moisture thresholds

244 Recall that soil moisture wilting point θ_w refers to the soil moisture level when ET ceases
 245 to occur, and the critical point θ_c refers to the soil moisture value that ET transforms from the
 246 energy-limited regime to water-limitation. In this case, the two thresholds correspond reasonably
 247 to the soil moisture values at both ends of the drydown events, i.e., θ_w and θ_c can be approximated

248 by statistics (e.g., median or mean) of $\widehat{\theta}_w$ in (2b) and the initial soil moisture ($\widehat{\theta}_p$) at the beginning
 249 of each identified drydown event, when the total number of identified drydown events are
 250 statistically sufficient (e.g., more than 50 events within 5 years at each grid). We here use multi-
 251 year medians of $\widehat{\theta}_w$ and $\widehat{\theta}_p$ instead of their means because they represent the majority of the
 252 analyzed variables (as opposed to mean values that could be biased by extremes) (Feldman et al.,
 253 2021), although we acknowledge that theoretically the truth of θ_w and θ_* can hardly be obtained
 254 by using observations only.

255 We also note that the soil moisture thresholds retrieved from soil moisture time series may
 256 not facilitate direct comparisons with those encoded in LSMs, which are typically prescribed or
 257 calculated dependent on soil texture data (e.g., through Pedo-Transfer Functions, PTF hereafter).
 258 Therefore, we also compare $\widehat{\theta}_w$ and $\widehat{\theta}_p$ with the soil moisture thresholds calculated from the Global
 259 Soil Dataset for Earth System Modeling (GSDE, Shangguan et al., 2014), a soil texture dataset
 260 that is prevalently used in many LSMs (e.g., Noah LSM with Multiple Parameters, Noah-MP (Niu
 261 et al., 2011; Yang et al., 2011)). We use the PTF from Saxton and Rawls (2006) to include the
 262 organic matter effects. Additional PTF function from Clapp and Hornberger (1978) is also
 263 analyzed. Details of PTF function can be found in Supplementary Materials (Table S1).

264

265 **3 Data**

266 **3.1 SMAP Surface Soil Moisture Data**

267 Five annual cycles (i.e., April 1, 2015 to March 31, 2020) of soil moisture retrievals from Soil
 268 Moisture Active and Passive Mission (SMAP, (Entekhabi et al., 2010)) are used to obtain satellite
 269 estimation of τ_S and τ_L respectively. SMAP measures soil moisture at the surface soil layer (i.e.,
 270 0 – 5cm) from the L-band microwave radiometer. Validated by a large number of ground
 271 observations, SMAP SSM has been shown to have high accuracy to capture soil moisture
 272 timeseries compared to other microwave soil moisture products. SMAP has a nominal revisiting
 273 period of 3 days at the equator (1~2 days in polar regions), therefore it performs well in
 274 characterizing land-atmosphere coupling processes at weekly and sub-weekly time scales. Here
 275 we choose soil moisture products derived from the Multi-Temporal Dual Channel Algorithm
 276 (MTDCA) (Konings et al., 2016) since it uses time-invariant scattering albedo, and therefore
 277 reduces high-frequency noises. The spatial resolution of MTDCA product used in this study is
 278 36km with EASE projections.

279 Prior to conducting the analysis, a quality control procedure has been applied to reduce the
 280 influences of noise encoded in satellite measurement. Consistent with several previous studies
 281 (McColl et al., 2019, 2017), soil moisture data over areas with dense vegetation cover (e.g.,
 282 vegetation water content $\geq 5 \text{ kg m}^{-2}$), intense Radio Frequency Interference (RFI), water bodies,
 283 and frozen landscapes are filtered. In addition, since the surface water balance is easily affected

284 by the temporal resolution of the analyzed SSM data, the SMAP soil moisture data are then
285 resampled to a uniform sampling frequency of $1/3 d^{-1}$ at each pixel (McColl et al., 2017).

286 **3.2 Reanalysis Datasets**

287 Surface soil moisture from six prevalent reanalysis datasets including Global Land Data
288 Assimilation System v2.2 Catchment Land Surface Model (GLDAS-CLSM (Li et al., 2020)) and
289 Global Land Data Assimilation System v2.1 Noah Model (GLDAS-Noah (Beaudoing, et al., 2020)
290) from Goddard Earth Science Data Information and Services Center (GES DISC) at the National
291 Aeronautics and Space Administration (NASA), Modern-Era Retrospective Analysis for Research
292 and Applications version2 (Merra2, (Gelaro et al., 2017)) from NASA's Global Modeling and
293 Assimilation (GMAO), National Centers for Environmental Prediction Final Operational Global
294 Analysis (NCEP-FNL, DOI: 10.5065/D6M043C6), European Center for Mesoscale Weather
295 Forecast, version5 (ERA5(Hersbach et al., 2020)), and Japanese 55-year Reanalysis (JRA55,
296 (Kobayashi et al., 2015)) from Japan Meteorological Agency are used to estimate soil moisture
297 memory at different time scales.

298 All reanalysis datasets employed in this study are listed in Table 1. Among them, four
299 distinctive LSMs, namely, the Catchment LSM, Noah LSM, (H)TSSEL and SiB are run with
300 coupling scheme (to atmosphere model) to produce soil moisture simulations for MERRA2,
301 NCEP, ERA5 and JRA55, respectively. Comparing soil memory analysis between these datasets
302 could inform the model-dependent L-A coupling characteristics (e.g., consistency and divergence
303 of LSMs' performance in L-A interactions). Two LSMs (i.e., Catchment and Noah LSMs) are run
304 with offline coupling scheme to provide soil moisture data for GLDAS-Catchment and GLDAS-
305 Noah. Comparing results from these two datasets with analyses from other LSMs can diagnose the
306 effects of atmospheric processes (e.g., moist convection and turbulence mixing) on L-A
307 interactions. We note that the soil layer depth is 10 cm in all datasets in this study, except for the
308 GLDAS-CLSM and JRA55, which has a topsoil layer of 2cm. Comparing memory results
309 estimated from these two models with others could inform the influence of soil depths on flux
310 exchanges at the land-atmosphere interface. All the soil moisture data are aggregated to a common

311 36 km spatial resolution, and their temporal resolutions are resampled to $1/3 \text{ day}^{-1}$, consistent to
 312 SMAP observations.

313 Table 1. Detailed information of six reanalysis datasets in this study

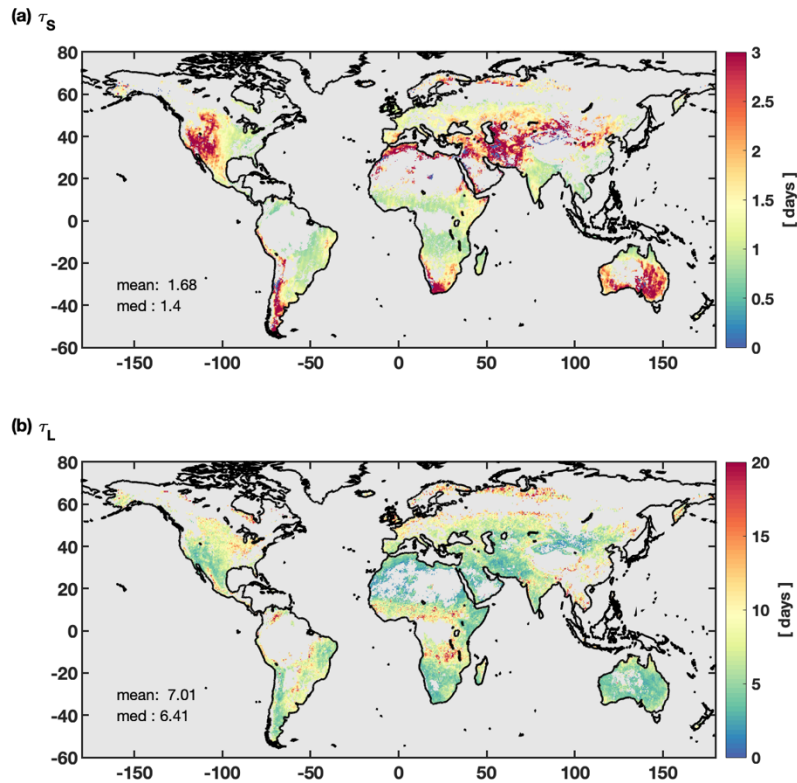
Data Names	LSMs	Surface Soil Layer Depth	Spatial Resolution	Temporal Resolution
GLDAS-CLSMv2.2	Catchment (offline)	0-2cm	$0.25^\circ \times 0.25^\circ$	1 day
GLDAS-Noahv2.1	Noah (offline)	0-10cm	$0.25^\circ \times 0.25^\circ$	3 hours
MERRA2	Catchment (coupled)	0-10cm	$0.625^\circ \times 0.5^\circ$	1 hour
NCEP	Noah (coupled)	0-10cm	$1^\circ \times 1^\circ$	6 hours
ERA5	(H)TESSEL (coupled)	0-10cm	$0.25^\circ \times 0.25^\circ$	1 hour
JRA55*	SiB (coupled)	0-2cm	$0.5^\circ \times 0.5^\circ$	3 hours

314

315 3.3 GPM Precipitation Data

316 Precipitation information is needed when calculating soil memory in the energy-limited
 317 regime (τ_S). Here, we use Late-Run Integrated Multi-Satellite Retrievals (IMERG) from NASA's
 318 Global Precipitation Mission (GPM) (Huffman et al., 2019). The IMERG product has a spatial
 319 resolution of 0.1° , and is regridded to 36km. The half-hourly data are then converted from UTC to
 320 daily 6 a.m. local time to be consistent with SMAP's overpass time. Similar to (McColl et al.,
 321 2019), the satellite-observed precipitation data, rather than the precipitation forcing that drives

322 LSMs, are used when estimating τ_S for the reanalysis datasets to isolate the impact of soil moisture
 323 on the comparison between observations and models.



324 Figure 2 Global distribution of energy-limited soil moisture memory (τ_S , (a)) and water-
 325 limited memory (τ_L , (b)) estimated from 5-year SMAP datasets. Inserted texts refer to global
 326 mean and median values.
 327

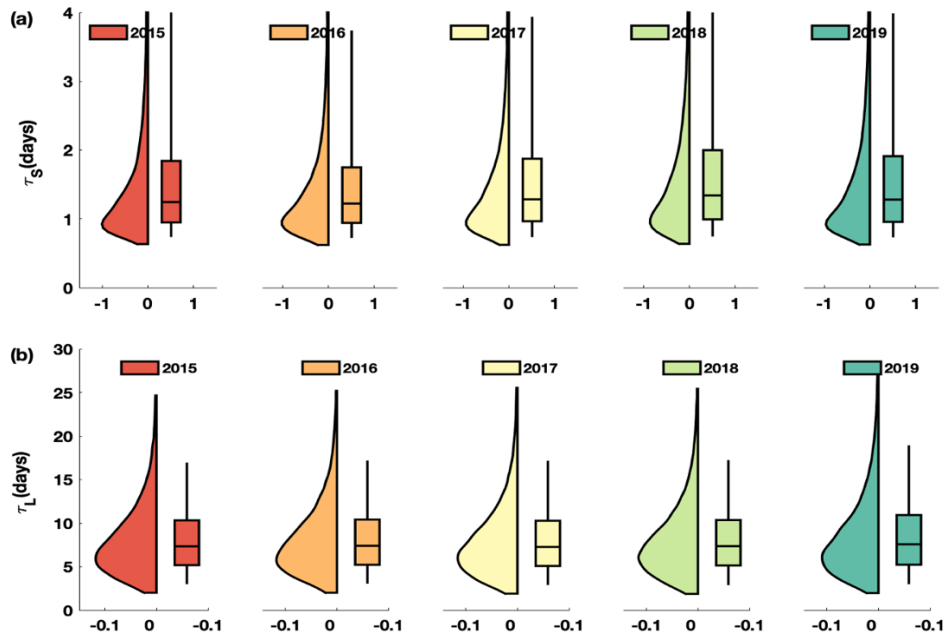
328 4 Results

329 4.1 τ_S and τ_L estimated from SMAP SSM data

330 Figure 2 shows the global distribution of median τ_L and τ_S estimated from 5-yr SMAP
 331 observations. At the global scale, the energy-limited soil memory time τ_S is longer over arid
 332 regions (such as the Midwest of the United States and central Australia) whereas the water-limited
 333 soil memory time τ_L is longer over wet areas, corresponding reasonably to the spatial distribution
 334 of soil hydraulic properties – the wet areas tend to have higher soil hydraulic conductivity thus
 335 precipitation drains more rapidly into the deep soils. The Spearman's correlation ($\rho = 0.51, p <$
 336 0.05) further suggests these two memory scales are spatially anti-correlated (Figure S1), which
 337 compare consistently to analyses reported in previous studies (McColl et al., 2017b, 2019).

338 In addition to the spatial pattern, we also analyze the temporal variability of τ_L and τ_S ,
 339 which has not yet gained particular concern in literature. We emphasize that the soil memory time
 340 discussed in this study are two proxies for measuring L-A coupling strength, therefore their
 341 temporal variability (e.g., year-to-year variations) may significantly change the spatial pattern and

342 frequency of the occurrences of extreme events. Figure 3 shows that annual variations of the soil
 343 memory time within the study period (i.e., 2015-2019). Results show that both τ_L and τ_S remain
 344 consistently unchanged within a rather long-term. Although the τ_L shows the longer-tailed
 345 distribution in the year 2019, the low density of τ_L with “extreme” values indicates this does not
 346 influence the overall distribution. These results indicate that the spatial pattern of different soil
 347 drying regimes remains qualitatively fixed and the drying rates do not change over time. Moreover,
 348 these results also suggest that the satellite estimates of τ_L and τ_S are robust and can serve as credible
 349 references to examine the L-A coupling strength in the reanalysis datasets.



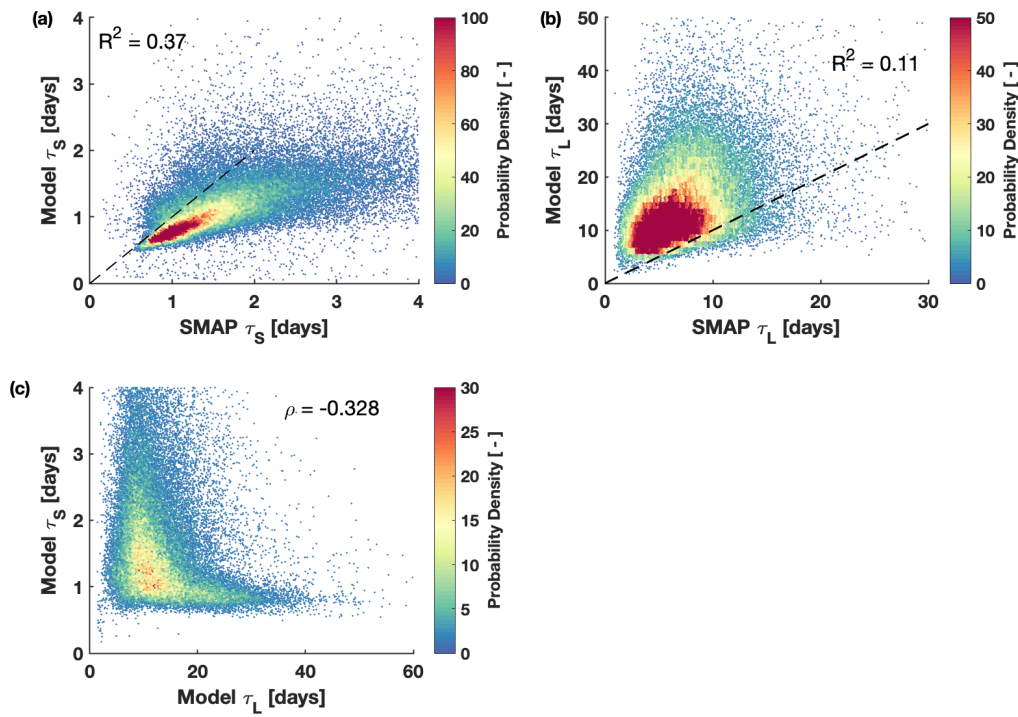
350

351 Figure 3 Annual variability of statistics for τ_S (above) and τ_L (below) estimated from SMAP observation.
 352 Polygons indicate Probability Density (PDF) curves.

353 4.2 τ_S and τ_L from reanalysis data

354 Figure 4 shows the scatterplots of the multi-model mean of τ_L and τ_S estimates, and their
 355 comparison with the SMAP observations, respectively. The global maps of multi-model means are
 356 shown in Figure S2 of the supplementary material. The results show that current LSMs can present
 357 reasonable anti-correlated patterns of τ_L and τ_S with Spearman's correlation of -0.37. The global
 358 multi-model mean maps also show that τ_S is longer in arid areas while long τ_L occurs in wet areas
 359 (Figure S2). However, by comparing τ_L and τ_S with satellite estimates, respectively, Figure 4a and
 360 Figure 4b show that the energy-limited soil memory is underestimated while the memory time at

361 the water-limited regime is overestimated, indicating that L-A processes at different time scales
 362 are generally misrepresented by LSMs.

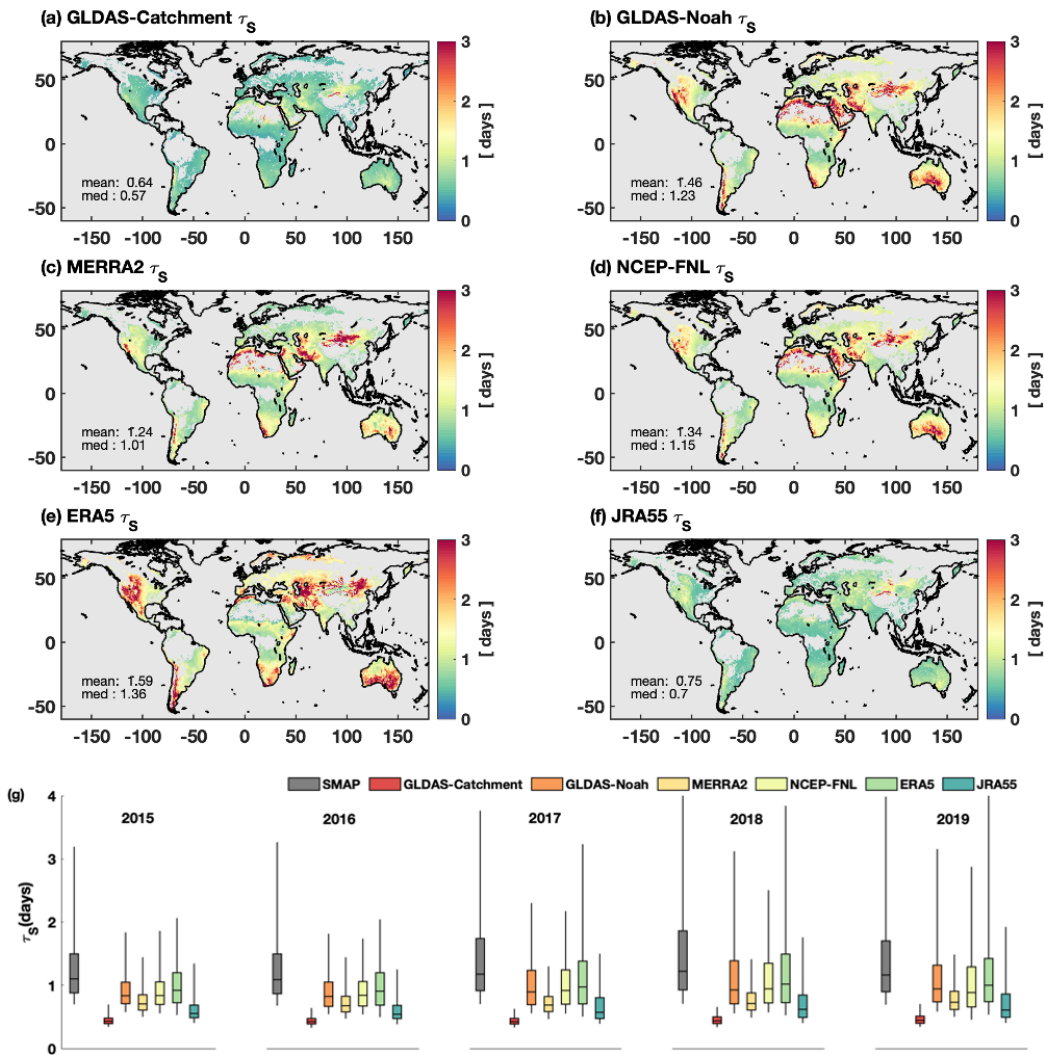


363

364 Figure 4 Scatterplots of multi-model mean of τ_S (a) and τ_L (b) versus SMAP estimation. (c) refer to the
 365 scatterplot between τ_S versus τ_L . Inserted texts are correlations between each pair of the analyzed
 366 variables. Colorbars indicates probability density.

367 There could be multiple reasons (e.g., model's physical parameterizations, coupling
 368 schemes, etc.) that can lead to memory biases in current LSMs. Individual models may thus
 369 perform strong disagreement in capturing L-A characteristics. Figure 5 and Figure 6 show the
 370 inter-comparison of τ_L and τ_S between six reanalysis datasets as well as SMAP observations,
 371 respectively. Consistent to the multi-model mean results, the six analyzed datasets all show
 372 substantial underestimations of τ_S and overestimation of τ_L compared to satellite estimates.
 373 However, the biases in model-estimated memory time show large model spreads. Specifically,
 374 GLDAS-CLSM and JRA55 present the two largest underestimations for the energy-limited
 375 memory time, with a median of 0.57 and 0.7 day compared to 1.4 days of SMAP estimates,
 376 respectively. The other four datasets show similar underestimations (Figure 5, b - e) of the τ_S
 377 results; however, the τ_S estimations of these four datasets compare more closely to SMAP, relevant
 378 to GLDAS-CLSM and JRA55. This could be relevant to soil depth. The topsoil depth prescribed
 379 in GLDAS-CLSM and JRA55 is 2cm, only one-fifth of those in other LSMs. Since τ_S reflects the
 380 soil water-holding capacity and is a direct function of soil layer thickness, it is not strange that a
 381 model with a thinner soil layer would exhibit more rapid drainage or ET-I drying rates. However,
 382 for the other models such as GLDAS-Noah, MERRA2, NCEP-FNL and ERA5, in which the soil

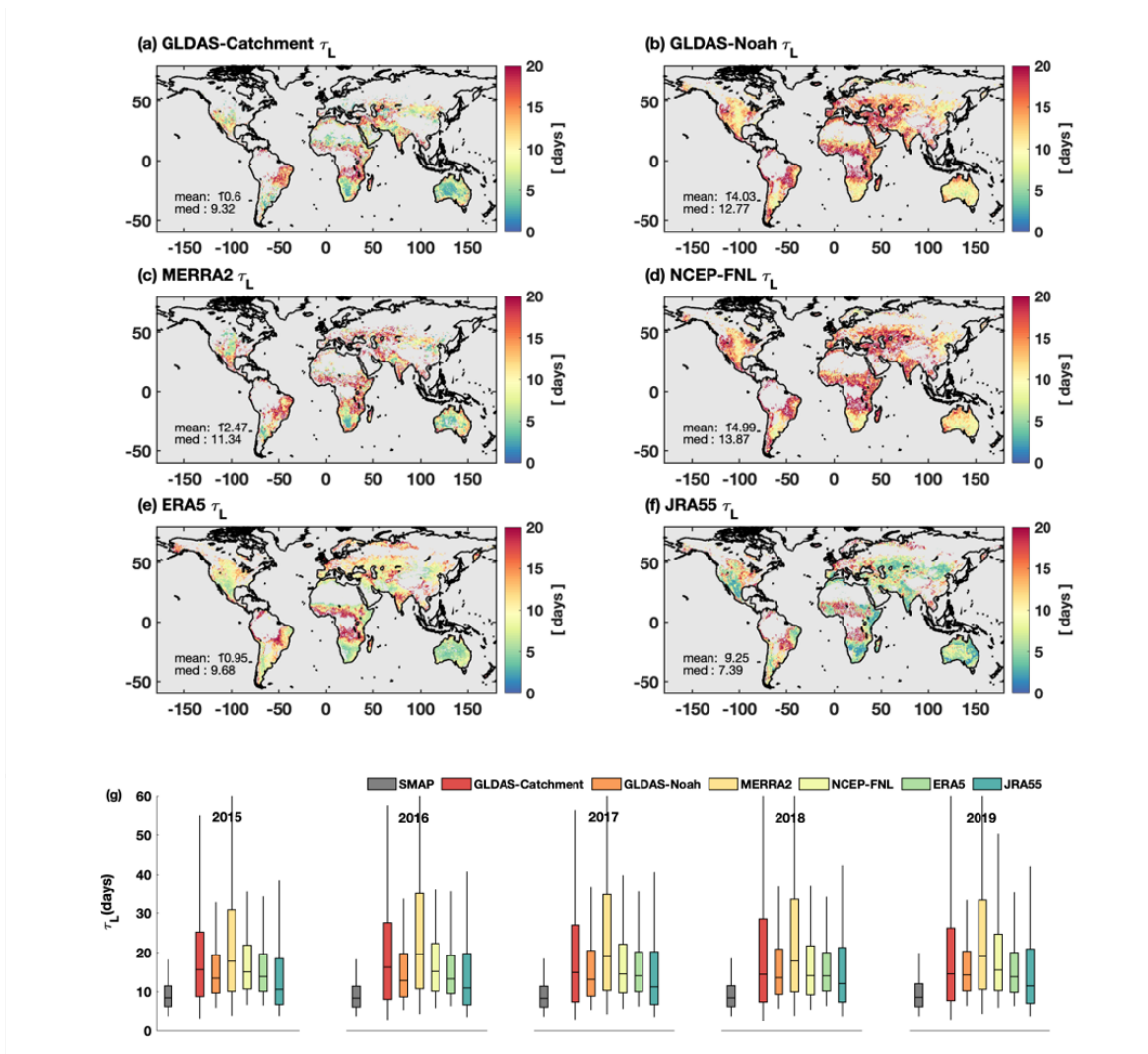
383 depths are twice as much as the nominal detecting depth of SMAP, τ_S estimates are still
 384 underestimated with medians around 0.3 day.



385
 386 Figure 5 Global distribution of τ_S for each individual model (a – f) and the annual
 387 variability of their statistics (g). Inserted texts in (a – f) refer to global mean and median
 388 values for each model.

389 Compared to τ_S results, the models show an overall overestimation of τ_L . In contrast to τ_S
 390 results, the model estimated τ_L also shows a large model spread but the inter-model comparison
 391 does not show high relevance to soil layer thickness. This may indicate that the water-limited
 392 processes, in particular, the stage-II ET process at the surface soil layer is more tightly related to
 393 deeper soils than the energy-limited processes such as drainage and runoff. The largest τ_L median
 394 overestimation is presented by MERRA2 instead of GLDAS-CLSM. Moderate τ_L biases are
 395 presented in GLDAS-Noah, NCEP-FNL and ERA5, with their medians more than twice as
 396 compared to SMAP observations. τ_L estimation from JRA55 shows to be the closest to SMAP

397 estimate, verifying that the parameterizations in SiB LSM perform better in the characterizations
 398 of water-limited soil drying processes.



399

400 Figure 6 Same as Figure 5 **Global distribution of τ_S for each individual model (a – f) and the**
 401 **annual variability of their statistics (g). Inserted texts in (a – f) refer to global mean and**
 402 **median values for each model, but for τ_L .**

403 In addition to the model dependence and soil layer depth, we also find that neither τ_S nor
 404 τ_L estimate is highly sensitive to the models' coupling schemes. For example, for GLDAS-Noah
 405 and NCEP-FNL, both of which use Noah LSM but are run with different coupling schemes, e.g.,
 406 the LSM is run offline in GLDAS-Noah while is coupled to the atmospheric model in NCEP-FNL,
 407 τ_S and τ_L both show similar statistics (e.g., medians, quantiles and ranges). While the memory
 408 results in the other pair (i.e., GLDAS-Catchment and MERRA2) show relatively larger
 409 differences, this discrepancy can be possibly attributed to the model's inconsistencies in soil layer
 410 thickness. By comparison, previous studies have shown that land properties (i.e., soil organic
 411 matter) can have different effects on surface states (e.g., soil temperature and near-surface air
 412 temperature) in coupled and uncoupled LSMs, respectively (citations, Sun et al., 202?). However,

413 we note that these analyses only focus on surface state variables rather than diagnostics related to
414 time-variant processes. Our results, by analyzing the soil drying time, show that the atmospheric
415 processes play minor roles in regulating land surface processes at time scales of hours to
416 subweekly. The above analyses suggest that the underestimation of SMM in current LSMs is not
417 caused by soil layer depths or the models' online/offline simulating schemes, but by other factors
418 such as the models' employment of physical parametrizations and static parameters (such as soil
419 and vegetation properties).

420 4.3 Terrestrial water cycle diagnostics informed by τ_S and τ_L

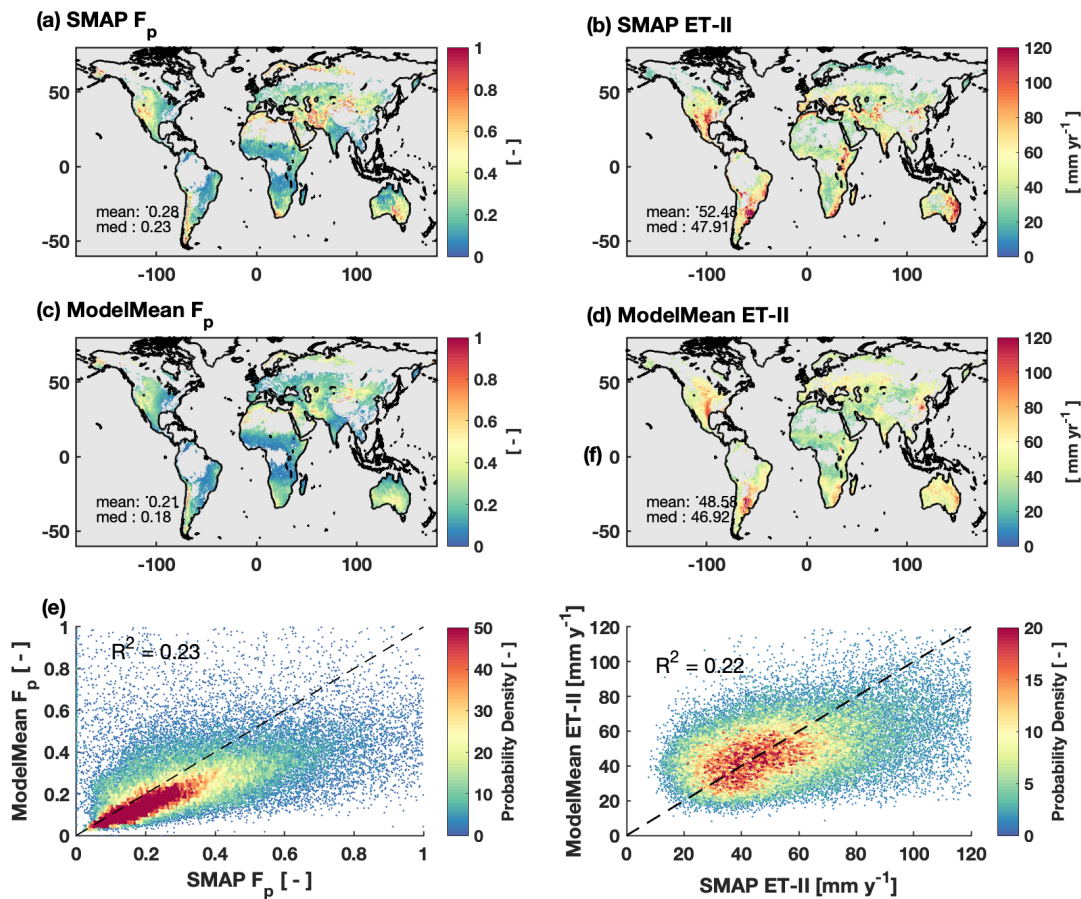
421 Figure 7 shows the comparison of F_p (left column) and Stage-II ET (right column)
422 estimation between multi-model mean and satellite-based estimations. Only four datasets with
423 equal soil layer depth (10 cm) are chosen here to represent the majority of the analyzed models
424 since ET is accumulated with soil layer depths. Results including GLDAS-CLSM and JRA55 are
425 shown in Figure S3 in the supplementary materials.

426 F_p estimate based on five-year SMAP SSM retrievals presents a similar global pattern, but
427 with a median of 23% compared to 14.4% reported in McColl et al (2017). Since F_p is essentially
428 relevant to "wet" risks (e.g., floods) at synoptic time scales (Liu et al., 2021), a 7% difference in
429 F_p may result in a different global pattern of water-related extreme events. This means the
430 comparison of F_p between the original SMAP soil moisture estimation and results from other
431 remote sensing products and climate models should be further validated. For example, Liu et al.
432 (2021) show that one current LSM (i.e., CLM) produces consistent F_p to satellite estimation.
433 Therefore, they use historical simulations from CLM as a baseline to compare with F_p projections
434 in future climate, and conclude that the precipitation retained in the surface soil layer could
435 possibly decrease. However, the multi-model mean estimate from four reanalysis datasets suggests
436 that current LSMs present an underestimation of F_p evaluated by both mean (21% of models vs.
437 28% of satellite) and median (18% of models vs. 23% of satellite) statistics. Results including all
438 datasets lead to a consistent conclusion. This result indicates that assessments of future F_p
439 projections may be re-examined with the historical reference redefined.

440 The annual Stage-II ET from a five-year SMAP estimation presents a global median of
441 47.91 mm yr⁻¹, showing several hotspots (e.g., Stage-II ET > 100 mm yr⁻¹) occurring in the central
442 US, South America, and eastern Australia. By comparison, the multi-model mean (of four analyzed
443 datasets) shows an underestimation of Stage-II ET with a global median of 39.67 mm yr⁻¹. Stage-
444 II ET of six-model-mean is even lower, with a global median of only 35.75 mm yr⁻¹. Particularly,
445 Stage-II ET hotspots (including the central US, which has previously been identified as one of the
446 regions that have the strongest L-A coupling strength on the globe by Koster et al. (2004)) are
447 muted in the multi-model mean results. The above results suggest that the flood risks are
448 underestimated in current LSMs, and the observed water-limitations on Stage-II ET are more
449 severe than characterized in models. As such, calibrating models' surface energy partitioning
450 processes (e.g., soil moisture and ET coupling regimes) with observed evidence may help to
451 improve models' representations of L-A interactions.

452 The F_p results show consistent model spread to Stage-II ET results as well as spread in
453 energy-limited soil moisture memory τ_S (Figure S4 and Figure S5). Still, the results are highly

454 sensitive to soil depth and models' parameterization schemes, but show insignificant sensitivity to
 455 models' coupling schemes. For example, both F_p and Stage-II ET from GLDAS-CLSM and JRA55
 456 are much lower than other models due to the soil depth configuration, and the differences between
 457 ERA5 and other models with consistent soil depth (i.e., GLDAS-Noah, MERRA2 and NCEP-
 458 FNL) are more distinctive than those between models with different coupling schemes (e.g.,
 459 MERRA2 and NCEP-FNL).



460

461 Figure 7 Global distribution of precipitation fraction (F_p , left column) and stage-II ET (right
 462 column) for multi-model mean (a – d), and their scatterplot versus SMAP estimations. Since ET
 463 is accumulated with soil layer depths, only four models with 10 cm soil layers are shown here.
 464 Results of including all models are shown in Figure S3.

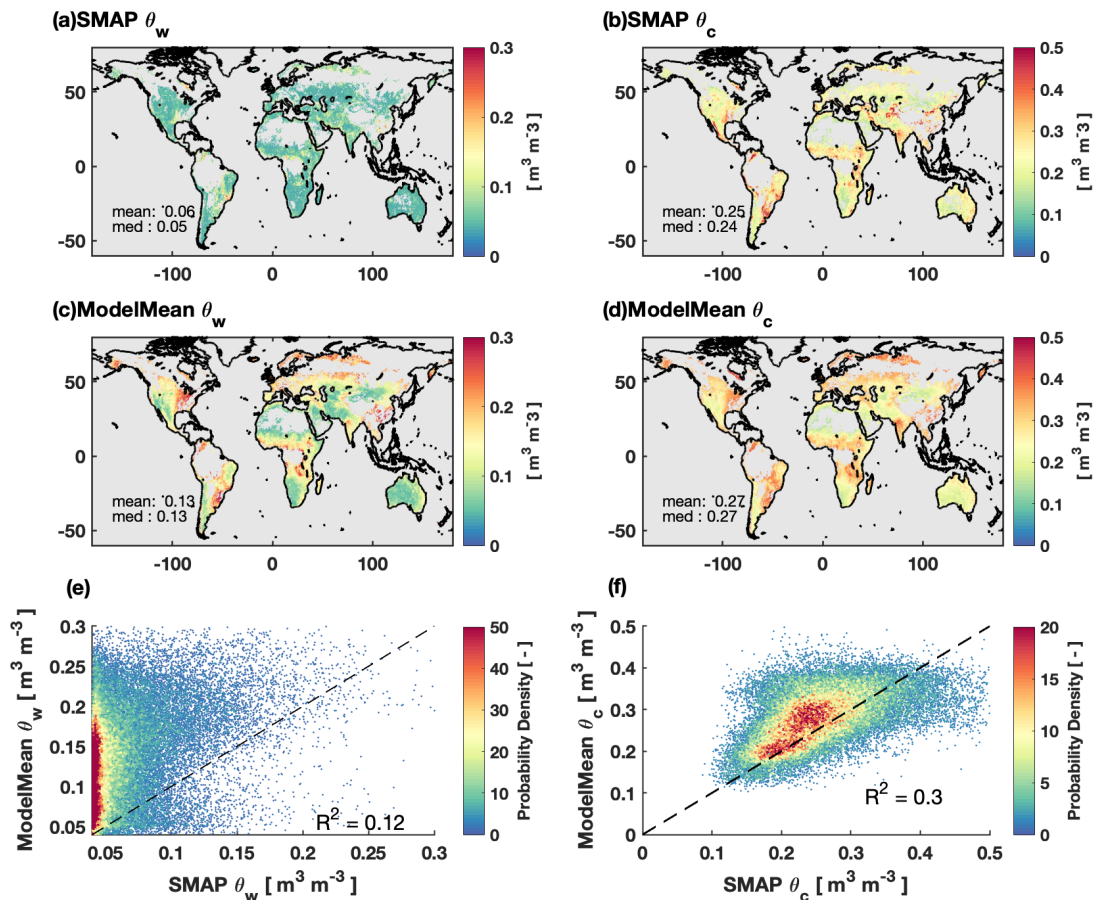
465 4.4 Critical soil moisture thresholds

466 The above results suggest that current LSMs' biases in L-A simulation are highly
 467 dependent on the models' parameterizations (including the physical schemes and the models' static
 468 parameters). However, systematically evaluating the effects of the models' physical schemes on
 469 the L-A coupling biases could be highly labor-intensive and time-consuming. Therefore, we chose
 470 to first evaluate one core component of the LSMs' static parameters, the soil hydraulic thresholds

471 because of their high relevance to SMM, to explore the essential factors that might contribute to
472 the models' L-A simulating biases.

473 Figure 8a and Figure 8c show the comparison of global soil wilting point θ_w between
474 SMAP observation and multi-model mean. The results show an overall similar global pattern, with
475 θ_w higher in strong L-A coupling hotspots. However, the SMAP observed θ_w shows much less
476 spatial heterogeneity, e.g., it has a narrower range (except for the hotspots, θ_w in most areas are
477 between $0.04 \text{ m}^3 \text{ m}^{-3}$ and $0.06 \text{ m}^3 \text{ m}^{-3}$). Comparison between the multi-model mean and the SMAP
478 observation shows that the models present a substantial overestimation of θ_w – the multi-model
479 mean shows a global median of $0.13 \text{ m}^3 \text{ m}^{-3}$ versus $0.05 \text{ m}^3 \text{ m}^{-3}$ of SMAP. The scatterplot further
480 validates the conclusion (Figure 8e). Similar overestimation is also observed in models' soil
481 moisture critical point θ_c (Figure 8b and Figure 8d). The global median θ_c of satellite-estimated
482 and multi-model mean are $0.24 \text{ m}^3 \text{ m}^{-3}$ and $0.27 \text{ m}^3 \text{ m}^{-3}$ respectively. In contrast to θ_w , the multi-

483 model mean of θ_c shows a particularly large overestimation in the strong L-A coupling areas.



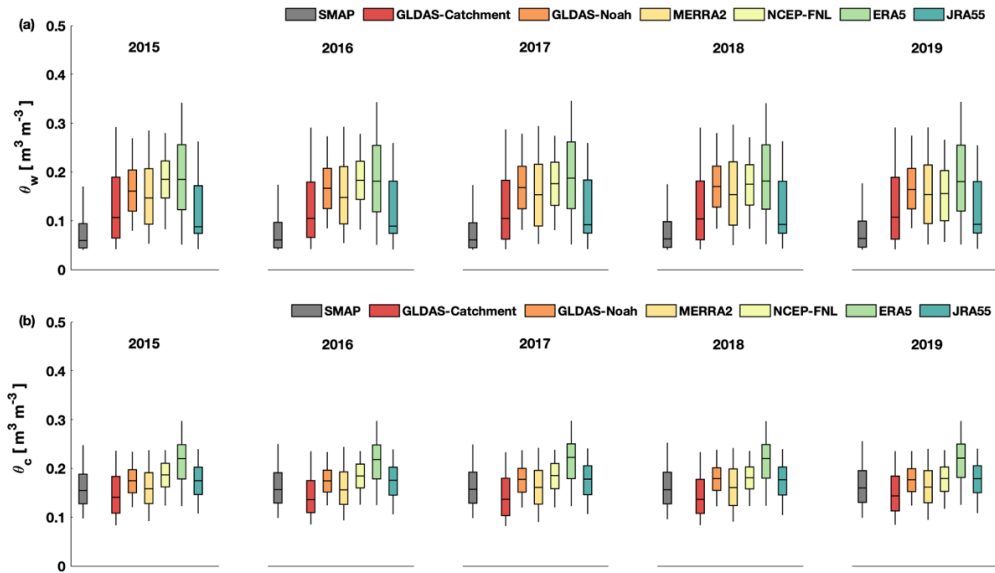
484

485 Figure 8 Global distribution of soil wilting point (θ_w , left column) and critical point (θ_c ,
 486 right column) for multi-model mean (a – d), and their scatterplot versus SMAP estimations.
 487 Areas where $\theta_w < 0.04 \text{ m}^3 \text{m}^{-3}$ are masked to mitigate noises induced by data quality.

488 Figure 9 shows the intercomparison of model spreads as well as the annual variability of
 489 θ_w and θ_c . Overall, the soil moisture thresholds estimated from models and satellite observation
 490 are robust within the five annual cycles. θ_w and θ_c of the models compare consistently
 491 overestimated to the SMAP observations. Intercomparison between individual models further
 492 shows that in contrast to soil memory and water cycle diagnostics, the soil moisture thresholds
 493 show minor sensitivity to models' soil layer depth or parameterization schemes. This indicates that
 494 the LSMs' L-A simulating biases may be commonly dominated by misrepresentations of soil
 495 hydraulic characteristics.

496 We note again the θ_w and θ_c retrieved from models' SM time series are not exactly the one
 497 that drives LSMs – soil parameters are often calculated from soil texture data in LSMs. Therefore,
 498 we compare the soil texture-based thresholds in order to diagnose possible reasons that may be
 499 responsible for uncertainties in models' L-A presentations. Figures S6-S7 show the global
 500 distribution of soil moisture thresholds calculated from GSDE soil texture data. The texture-based

501 θ_w and θ_c compare similarly to the thresholds retrieved from models' soil moisture timeseries and
 502 show consistent differences to the SMAP estimations. Comparison with thresholds calculated from
 503 Clapp and Hornberger (1978) scheme results in a consistent conclusion (Figure S8-S9). The
 504 similarity between retrieved- and texture-based results and their differences from satellite
 505 estimations suggest that the soil moisture thresholds could be highly relevant to the models' L-A
 506 coupling simulations, especially for simulations related to the energy-limited processes. Therefore,
 507 calibrating the soil texture datasets based on large-scale observational soil hydraulic thresholds
 508 may provide an efficient approach to improve the models' performances in L-A coupling
 509 simulations.



510

511 Figure 9 Annual variability of statistics for θ_w (above) and θ_c (below) of each individual models.

512 5 Conclusions

513 This study provides global evaluations of surface soil memory in six prevalently-used
 514 reanalysis datasets by using multi-year satellite estimations. The results show that the multi-model
 515 mean presents an overestimation of water-limited soil memory τ_L whereas tends to underestimate
 516 the energy-limited soil memory τ_S , suggesting that the soil memory biases reported previously in
 517 one or two example model(s) are prevalent in current LSMs. Large model spreads are observed
 518 between individual models, where the soil memory biases are highly dependent on models'
 519 parameterizations such as the static soil hydraulic property data, while showing minor relevance
 520 to the models' soil layer depth or online/offline simulating schemes.

521 Our study also provides a satellite-based estimation of two important terrestrial water
 522 cycle-related variables (i.e., the precipitation fraction F_p for assessing flood risks and water-limited
 523 evapotranspiration ET-II) at the global scale. The five-year mean F_p presents a 7% increase (i.e.,
 524 the newly estimated F_p is 23%) in the global median to the originally reported results, indicating
 525 moderate sensitivity of observed flood risks to the remote sensing products. This also suggests that
 526 future assessments of F_p , as well as flood risks in climate models, should consider factors such as

527 the robustness of the reference F_p datasets. The satellite estimation of ET-II shows reasonable
528 spatial distribution compared to the observed pattern of strong L-A coupling regions. Compared
529 to prevailing ET products, the advantage of ET-II in our study is that we separate ET limited by
530 surface water availability from the ET partitioning processes with explicit physical meaning. As
531 ET partitioning regulates carbon redistribution of plants, and energy and water exchanges between
532 land and near-surface atmosphere (Akbar et al., 2019; Feldman et al., 2020, 2019; Williams and
533 Torn, 2015; Zhou et al., 2016), calibrating the physical parameterizations such as surface resistance
534 or carbon assimilation schemes with satellite-observed Stage-II ET may improve the simulations
535 of L-A coupling variables (e.g., soil moisture and temperature) and vegetation dynamics (e.g.,
536 Gross Primary Production, Transpiration-ET ratio) in LSMs.

537 Global satellite-based soil hydraulic parameters (i.e., the soil moisture wilting point θ_w and
538 critical point θ_c) are finally provided. The θ_w and θ_c statistics are robust within five annual cycles.
539 The multi-model results show substantial differences in both θ_w and θ_c from the satellite
540 estimates. Comparison with texture-based analysis confirms the conclusion. Large-scale products
541 of soil hydraulic parameters are typically provided by extrapolating in-situ measurements from
542 geographical survey records, where the data quality is only vaguely defined (Bouma, 1989; Dai et
543 al., 2019). Our study, by comparing global observational evidence, further shows that the texture-
544 based estimations of θ_w and θ_c are both overestimated. Furthermore, the soil hydraulic parameters
545 are directly related to soil texture. As such, the results indicate the soil texture information may be
546 improved by optimizing from satellite-observed θ_w and θ_c , and thus could enable considerable
547 improvements of the equilibrium soil moisture simulation biases in many LSMs.

548 Several limitations, however, should also be addressed in this study. ET-II and soil
549 moisture thresholds θ_w and θ_c are both estimated by characterizing soil moisture drydown curves.
550 The method itself contains uncertainty. For example, when fitting the drydown timeseries, the
551 functional forms, e.g., using the logarithmic function instead of the exponential function, may lead
552 to different estimations. However, updating the fitting function would need additional hypotheses
553 and may bring in extra uncertainty, and the derivation of a new method to characterize the drydown
554 processes is beyond the scope of this study. The parameter boundaries (e.g., the minimum soil
555 moisture values, and upper and lower boundary limits of constants in the fitting procedure) would
556 also lead to different results. However, we have tested the fitting procedure by changing boundary
557 limits, and the results show that the influence on parameters is minor (not shown).

558 Another factor that may affect the results is the soil moisture sampling frequency. The
559 sampling frequency used in this study is $1/3 \text{ d}^{-1}$ (reverse of SMAP's nominal revisiting period),
560 therefore different estimations of soil memory as well as relevant diagnostics should be expected
561 when land processes occurred within 3 days are included. In addition, 5-year soil moisture data
562 may still be insufficient to produce a robust estimate of these variables. Sensitivity of ET-II and
563 soil moisture thresholds to these factors are thus expected by using soil moisture datasets with
564 higher sampling frequency and long temporal coverage available (e.g., a recently developed soil
565 moisture datasets from the neural network (Yao et al., 2021) provides daily satellite-based soil
566 moisture products with 20-year temporal coverage). However, we emphasize that the primary aim
567 of this study is to provide evaluations of L-A coupling performance in several prevalently-used
568 reanalysis datasets with satellite-observed evidence. However, since credible L-A products are
569 essentially important for improvements in current LSMs, future practices are heartily expected to
570 produce such datasets with high and robust data quality.

571

572 **Acknowledgments**

573 This study is supported by the National Key Research and Development Program of China
574 (2017YFA0603703), the Second Tibetan Plateau Scientific Expedition and Research Program
575 (STEP, grant No. 2019QZKK0206), and the International Partnership Program of Chinese
576 Academy of Sciences (182211KYSB20200015). We thank Andrew Feldman for providing the
577 MTDCA soil moisture data.

578

579 **Open Research**

580 SMAP soil moisture data are available at <https://doi.org/10.6084/m9.figshare.21184366.v1> ;
581 GLDAS-CLSMv2.2 datasets are available from
582 https://disc.gsfc.nasa.gov/datasets/GLDAS_CLSM025_DA1_D_2.2/summary?keywords=GLDA
583 [S](#) . GLDAS-Noah data are available from
584 https://disc.gsfc.nasa.gov/datasets/GLDAS_NOAH025_3H_2.1/summary?keywords=GLDAS ;
585 MERRA2 is available from https://disc.gsfc.nasa.gov/datasets/M2T1NXLND_5.12.4/summary ;
586 NCEP-FNL is available from <https://rda.ucar.edu/datasets/ds083.2/> ; ERA5 is available from
587 <https://cds.climate.copernicus.eu/cdsapp#!/dataset/reanalysis-era5-single-levels?tab=overview> ;
588 JRA55 is available from <https://rda.ucar.edu/datasets/ds628.0/> ; GPM precipitation data is
589 available from https://gpm1.gesdisc.eosdis.nasa.gov/data/GPM_L3/GPM_3IMERGHH.06/ ;
590 GSDE soil texture data is available from <http://globalchange.bnu.edu.cn/research/soilw> .

591

592 **References**

593 Akbar, R., Short Gianotti, D.J., Salvucci, G.D., Entekhabi, D., 2019. Mapped Hydroclimatology of
594 Evapotranspiration and Drainage Runoff Using SMAP Brightness Temperature

- 595 Observations and Precipitation Information. *Water Resour. Res.* 55, 3391–3413.
596 <https://doi.org/10.1029/2018WR024459>
- 597 Beaudoin, H., Rodell, M., NASA/GSFC/HSL, 2020. GLDAS Noah Land Surface Model L4 3 hourly
598 0.25 x 0.25 degree, Version 2.1. <https://doi.org/10.5067/E7TYRXPJKWOQ>
- 599 Berg, A., Sheffield, J., 2018. Soil Moisture–Evapotranspiration Coupling in CMIP5 Models:
600 Relationship with Simulated Climate and Projections. *Journal of Climate* 31, 4865–4878.
601 <https://doi.org/10.1175/JCLI-D-17-0757.1>
- 602 Bouma, J., 1989. Using Soil Survey Data for Quantitative Land Evaluation, in: Lal, R., Stewart,
603 B.A. (Eds.), *Soil Restoration, Advances in Soil Science*. Springer New York, New York, NY,
604 pp. 177–213. https://doi.org/10.1007/978-1-4612-3532-3_4
- 605 Clapp, R.B., Hornberger, G.M., 1978. Empirical equations for some soil hydraulic properties.
606 *Water Resour. Res.* 14, 601–604. <https://doi.org/10.1029/WR014i004p00601>
- 607 Dai, Y., Shangguan, W., Wei, N., Xin, Q., Yuan, H., Zhang, S., Liu, S., Lu, X., Wang, D., Yan, F.,
608 2019. A review of the global soil property maps for Earth system models. *SOIL* 5, 137–
609 158. <https://doi.org/10.5194/soil-5-137-2019>
- 610 Delworth, T.L., Manabe, S., 1988. The Influence of Potential Evaporation on the Variabilities of
611 Simulated Soil Wetness and Climate. *J. Climate* 1, 523–547.
- 612 Dirmeyer, P.A., 2011. The terrestrial segment of soil moisture–climate coupling: SOIL
613 MOISTURE–CLIMATE COUPLING. *Geophysical Research Letters* 38, n/a–n/a.
614 <https://doi.org/10.1029/2011GL048268>
- 615 Dirmeyer, P.A., Koster, R.D., Guo, Z., 2006. Do Global Models Properly Represent the Feedback
616 between Land and Atmosphere? *J. Hydrometeorol* 7, 1177–1198.
617 <https://doi.org/10.1175/JHM532.1>
- 618 Dirmeyer, P.A., Schlosser, C.A., Brubaker, K.L., 2009. Precipitation, Recycling, and Land Memory:
619 An Integrated Analysis. *Journal of Hydrometeorology* 10, 278–288.
620 <https://doi.org/10.1175/2008JHM1016.1>
- 621 Entekhabi, D., Njoku, E.G., O’Neill, P.E., Kellogg, K.H., Crow, W.T., Edelstein, W.N., Entin, J.K.,
622 Goodman, S.D., Jackson, T.J., Johnson, J., Kimball, J., Piepmeier, J.R., Koster, R.D.,
623 Martin, N., McDonald, K.C., Moghaddam, M., Moran, S., Reichle, R., Shi, J.C., Spencer,
624 M.W., Thurman, S.W., Tsang, L., Van Zyl, J., 2010. The Soil Moisture Active Passive
625 (SMAP) Mission. *Proc. IEEE* 98, 704–716. <https://doi.org/10.1109/JPROC.2010.2043918>
- 626 Feldman, A.F., Short Gianotti, D.J., Konings, A.G., Gentine, P., Entekhabi, D., 2021. Patterns of
627 plant rehydration and growth following pulses of soil moisture availability.
628 *Biogeosciences* 18, 831–847. <https://doi.org/10.5194/bg-18-831-2021>
- 629 Feldman, A.F., Short Gianotti, D.J., Trigo, I.F., Salvucci, G.D., Entekhabi, D., 2020. Land-
630 Atmosphere Drivers of Landscape-Scale Plant Water Content Loss. *Geophys. Res. Lett.*
631 47. <https://doi.org/10.1029/2020GL090331>
- 632 Feldman, A.F., Short Gianotti, D.J., Trigo, I.F., Salvucci, G.D., Entekhabi, D., 2019. Satellite-Based
633 Assessment of Land Surface Energy Partitioning–Soil Moisture Relationships and Effects
634 of Confounding Variables. *Water Resour. Res.* 55, 10657–10677.
635 <https://doi.org/10.1029/2019WR025874>
- 636 Gallego-Elvira, B., Taylor, C.M., Harris, P.P., Ghent, D., Veal, K.L., Folwell, S.S., 2016. Global
637 observational diagnosis of soil moisture control on the land surface energy balance.
638 *Geophys. Res. Lett.* 43, 2623–2631. <https://doi.org/10.1002/2016GL068178>

- 639 Gelaro, R., McCarty, W., Suárez, M.J., Todling, R., Molod, A., Takacs, L., Randles, C.A.,
640 Darmenov, A., Bosilovich, M.G., Reichle, R., Wargan, K., Coy, L., Cullather, R., Draper, C.,
641 Akella, S., Buchard, V., Conaty, A., da Silva, A.M., Gu, W., Kim, G.-K., Koster, R., Lucchesi,
642 R., Merkova, D., Nielsen, J.E., Partyka, G., Pawson, S., Putman, W., Rienecker, M.,
643 Schubert, S.D., Sienkiewicz, M., Zhao, B., 2017. The Modern-Era Retrospective Analysis
644 for Research and Applications, Version 2 (MERRA-2). *J. Climate* 30, 5419–5454.
645 <https://doi.org/10.1175/JCLI-D-16-0758.1>
- 646 Ghannam, K., Nakai, T., Paschalis, A., Oishi, C.A., Kotani, A., Igarashi, Y., Kumagai, T., Katul, G.G.,
647 2016. Persistence and memory timescales in root-zone soil moisture dynamics. *Water*
648 *Resour. Res.* 52, 1427–1445. <https://doi.org/10.1002/2015WR017983>
- 649 Guo, Z., Dirmeyer, P.A., Koster, R.D., Sud, Y.C., Bonan, G., Oleson, K.W., Chan, E., Versegny, D.,
650 Cox, P., Gordon, C.T., McGregor, J.L., Kanae, S., Kowalczyk, E., Lawrence, D., Liu, P.,
651 Mocko, D., Lu, C.-H., Mitchell, K., Malyshev, S., McAvaney, B., Oki, T., Yamada, T.,
652 Pitman, A., Taylor, C.M., Vasic, R., Xue, Y., 2006. GLACE: The Global Land–Atmosphere
653 Coupling Experiment. Part II: Analysis. *J. Hydrometeorol* 7, 611–625.
654 <https://doi.org/10.1175/JHM511.1>
- 655 Hersbach, H., Bell, B., Berrisford, P., Hirahara, S., Horányi, A., Muñoz-Sabater, J., Nicolas, J.,
656 Peubey, C., Radu, R., Schepers, D., Simmons, A., Soci, C., Abdalla, S., Abellan, X.,
657 Balsamo, G., Bechtold, P., Biavati, G., Bidlot, J., Bonavita, M., Chiara, G., Dahlgren, P.,
658 Dee, D., Diamantakis, M., Dragani, R., Flemming, J., Forbes, R., Fuentes, M., Geer, A.,
659 Haimberger, L., Healy, S., Hogan, R.J., Hólm, E., Janisková, M., Keeley, S., Laloyaux, P.,
660 Lopez, P., Lupu, C., Radnoti, G., Rosnay, P., Rozum, I., Vamborg, F., Villaume, S., Thépaut,
661 J., 2020. The ERA5 global reanalysis. *Q.J.R. Meteorol. Soc.* 146, 1999–2049.
662 <https://doi.org/10.1002/qj.3803>
- 663 Hu, G., Jia, L., 2015. Monitoring of Evapotranspiration in a Semi-Arid Inland River Basin by
664 Combining Microwave and Optical Remote Sensing Observations. *Remote Sensing* 7,
665 3056–3087. <https://doi.org/10.3390/rs70303056>
- 666 Huffman, G.J., Stocker, E.F., Bolvin, D.T., Nelkin, E.J., Tan, J., Savtchenko, A., 2019. GPM IMERG
667 Final Precipitation L3 1 day 0.1 degree x 0.1 degree V06.
- 668 Katul, G.G., Porporato, A., Daly, E., Oishi, A.C., Kim, H.-S., Stoy, P.C., Juang, J.-Y., Siqueira, M.B.,
669 2007. On the spectrum of soil moisture from hourly to interannual scales: SPECTRUM OF
670 SOIL MOISTURE CONTENT. *Water Resour. Res.* 43.
671 <https://doi.org/10.1029/2006WR005356>
- 672 Kim, H., Lakshmi, V., 2019. Global Dynamics of Stored Precipitation Water in the Topsoil Layer
673 From Satellite and Reanalysis Data. *Water Resources Research* 55, 3328–3346.
674 <https://doi.org/10.1029/2018WR023166>
- 675 Kobayashi, S., Ota, Y., Harada, Y., Ebita, A., Moriya, M., Onoda, H., Onogi, K., Kamahori, H.,
676 Kobayashi, C., Endo, H., Miyaoka, K., Takahashi, K., 2015. The JRA-55 Reanalysis: General
677 Specifications and Basic Characteristics. *Journal of the Meteorological Society of Japan*
678 93, 5–48. <https://doi.org/10.2151/jmsj.2015-001>
- 679 Konings, A.G., Piles, M., Rötzer, K., McColl, K.A., Chan, S.K., Entekhabi, D., 2016. Vegetation
680 optical depth and scattering albedo retrieval using time series of dual-polarized L-band
681 radiometer observations. *Remote Sensing of Environment* 172, 178–189.
682 <https://doi.org/10.1016/j.rse.2015.11.009>

- 683 Koster, R.D., 2004. Regions of Strong Coupling Between Soil Moisture and Precipitation. *Science*
684 305, 1138–1140. <https://doi.org/10.1126/science.1100217>
- 685 Koster, R.D., Dirmeyer, P.A., Hahmann, A.N., Ijpeelaar, R., Tyahla, L., Cox, P., Suarez, M.J., 2002.
686 Comparing the Degree of Land–Atmosphere Interaction in Four Atmospheric General
687 Circulation Models. *J. Hydrometeor.* 3, 363–375. [https://doi.org/10.1175/1525-
688 7541\(2002\)003<0363:CTDOLA>2.0.CO;2](https://doi.org/10.1175/1525-7541(2002)003<0363:CTDOLA>2.0.CO;2)
- 689 Koster, R.D., Schubert, S.D., Suarez, M.J., 2009. Analyzing the Concurrence of Meteorological
690 Droughts and Warm Periods, with Implications for the Determination of Evaporative
691 Regime. *Journal of Climate* 22, 3331–3341. <https://doi.org/10.1175/2008JCLI2718.1>
- 692 Koster, R.D., Suarez, M.J., 2001. Soil moisture memory in climate models. *J. Climate* 2, 558–570.
693 [https://doi.org/10.1175/1525-7541\(2001\)002<0558:SMMICM>2.0.CO;2](https://doi.org/10.1175/1525-7541(2001)002<0558:SMMICM>2.0.CO;2)
- 694 Koster, R.D., Sud, Y.C., Guo, Z., Dirmeyer, P.A., Bonan, G., Oleson, K.W., Chan, E., Versegny, D.,
695 Cox, P., Davies, H., Kowalczyk, E., Gordon, C.T., Kanae, S., Lawrence, D., Liu, P., Mocko,
696 D., Lu, C.-H., Mitchell, K., Malyshev, S., McAvaney, B., Oki, T., Yamada, T., Pitman, A.,
697 Taylor, C.M., Vasic, R., Xue, Y., 2006. GLACE: The Global Land–Atmosphere Coupling
698 Experiment. Part I: Overview. *J. Hydrometeor.* 7, 590–610.
699 <https://doi.org/10.1175/JHM510.1>
- 700 Li, Bailing, Beaudoin, H., Rodell, M., NASA/GSFC/HSL, 2020. GLDAS Catchment Land Surface
701 Model L4 daily 0.25 x 0.25 degree GRACE-DA1 Early Product, Version 2.2.
702 <https://doi.org/10.5067/IIU5JWU2AGRP>
- 703 Liu, X., Yuan, X., Zhu, E., 2021. Global warming induces significant changes in the fraction of
704 stored precipitation in the surface soil. *Global and Planetary Change* 103616.
705 <https://doi.org/10.1016/j.gloplacha.2021.103616>
- 706 Martínez-Fernández, J., González-Zamora, A., Almendra-Martín, L., 2020. Soil moisture memory
707 and soil properties: An analysis with the stored precipitation fraction. *Journal of*
708 *Hydrology* 125622. <https://doi.org/10.1016/j.jhydrol.2020.125622>
- 709 McColl, K.A., Alemohammad, S.H., Akbar, R., Konings, A.G., Yueh, S., Entekhabi, D., 2017a. The
710 global distribution and dynamics of surface soil moisture. *Nature Geosci* 10, 100–104.
711 <https://doi.org/10.1038/ngeo2868>
- 712 McColl, K.A., He, Q., Lu, H., Entekhabi, D., 2019a. Short-Term and Long-Term Surface Soil
713 Moisture Memory Time Scales Are Spatially Anticorrelated at Global Scales. *J.*
714 *Hydrometeor.* 20, 1165–1182. <https://doi.org/10.1175/JHM-D-18-0141.1>
- 715 McColl, K.A., He, Q., Lu, H., Entekhabi, D., 2019b. Short-Term and Long-Term Surface Soil
716 Moisture Memory Time Scales Are Spatially Anticorrelated at Global Scales. *J.*
717 *Hydrometeor.* 20, 1165–1182. <https://doi.org/10.1175/JHM-D-18-0141.1>
- 718 McColl, K.A., Wang, W., Peng, B., Akbar, R., Short Gianotti, D.J., Lu, H., Pan, M., Entekhabi, D.,
719 2017b. Global characterization of surface soil moisture drydowns: SURFACE SOIL
720 MOISTURE DRYDOWN ANALYSIS. *Geophys. Res. Lett.* 44, 3682–3690.
721 <https://doi.org/10.1002/2017GL072819>
- 722 Miralles, D.G., Gentile, P., Seneviratne, S.I., Teuling, A.J., 2019. Land-atmospheric feedbacks
723 during droughts and heatwaves: state of the science and current challenges: Land
724 feedbacks during droughts and heatwaves. *Ann. N.Y. Acad. Sci.* 1436, 19–35.
725 <https://doi.org/10.1111/nyas.13912>

- 726 Miralles, D.G., Teuling, A.J., van Heerwaarden, C.C., Vilà-Guerau de Arellano, J., 2014. Mega-
727 heatwave temperatures due to combined soil desiccation and atmospheric heat
728 accumulation. *Nature Geosci* 7, 345–349. <https://doi.org/10.1038/ngeo2141>
- 729 Mu, Q., Heinsch, F.A., Zhao, M., Running, S.W., 2007. Development of a global
730 evapotranspiration algorithm based on MODIS and global meteorology data. *Remote*
731 *Sensing of Environment* 111, 519–536. <https://doi.org/10.1016/j.rse.2007.04.015>
- 732 Mu, Q., Zhao, M., Steven, W., 2014. Running and Numerical Terradynamic Simulation Group:
733 MODIS Global Terrestrial Evapotranspiration (ET) Product MOD16A2 Collection 5.
- 734 Niu, G.-Y., Yang, Z.-L., Mitchell, K.E., Chen, F., Ek, M.B., Barlage, M., Kumar, A., Manning, K.,
735 Niyogi, D., Rosero, E., Tewari, M., Xia, Y., 2011. The community Noah land surface model
736 with multiparameterization options (Noah-MP): 1. Model description and evaluation
737 with local-scale measurements. *J. Geophys. Res.* 116, D12109.
738 <https://doi.org/10.1029/2010JD015139>
- 739 Pastorello, G., Trotta, C., Canfora, E., Chu, H., Papale, D., 2020. The FLUXNET2015 dataset and
740 the ONEFlux processing pipeline for eddy covariance data. *Scientific Data* 7.
741 <https://doi.org/10.1038/s41597-020-0534-3>
- 742 Saxton, K.E., Rawls, W.J., 2006. Soil Water Characteristic Estimates by Texture and Organic
743 Matter for Hydrologic Solutions. *Soil Sci. Soc. Am. J.* 70, 1569–1578.
744 <https://doi.org/10.2136/sssaj2005.0117>
- 745 Schwingshackl, C., Hirschi, M., Seneviratne, S.I., 2017. Quantifying Spatiotemporal Variations of
746 Soil Moisture Control on Surface Energy Balance and Near-Surface Air Temperature.
747 *Journal of Climate* 30, 7105–7124. <https://doi.org/10.1175/JCLI-D-16-0727.1>
- 748 Seneviratne, S.I., Corti, T., Davin, E.L., Hirschi, M., Jaeger, E.B., Lehner, I., Orlowsky, B., Teuling,
749 A.J., 2010. Investigating soil moisture–climate interactions in a changing climate: A
750 review. *Earth-Science Reviews* 99, 125–161.
751 <https://doi.org/10.1016/j.earscirev.2010.02.004>
- 752 Seneviratne, S.I., Lüthi, D., Litschi, M., Schär, C., 2006. Land–atmosphere coupling and climate
753 change in Europe. *Nature* 443, 205–209. <https://doi.org/10.1038/nature05095>
- 754 Shangguan, W., Dai, Y., Duan, Q., Liu, B., Yuan, H., 2014. A global soil data set for earth system
755 modeling. *J. Adv. Model. Earth Syst.* 6, 249–263.
756 <https://doi.org/10.1002/2013MS000293>
- 757 Williams, I.N., Torn, M.S., 2015. Vegetation controls on surface heat flux partitioning, and land-
758 atmosphere coupling: VEGETATION AND LAND-ATMOSPHERE COUPLING. *Geophys. Res.*
759 *Lett.* 42, 9416–9424. <https://doi.org/10.1002/2015GL066305>
- 760 Yang, Z.-L., Niu, G.-Y., Mitchell, K.E., Chen, F., Ek, M.B., Barlage, M., Longuevergne, L., Manning,
761 K., Niyogi, D., Tewari, M., Xia, Y., 2011. The community Noah land surface model with
762 multiparameterization options (Noah-MP): 2. Evaluation over global river basins. *J.*
763 *Geophys. Res.* 116, D12109. <https://doi.org/10.1029/2010JD015139>
- 764 Yao, P., Lu, H., Shi, J., Zhao, T., Yang, K., Cosh, M.H., Gianotti, D.J.S., Entekhabi, D., 2021. A long
765 term global daily soil moisture dataset derived from AMSR-E and AMSR2 (2002–2019).
766 *Sci Data* 8, 143. <https://doi.org/10.1038/s41597-021-00925-8>
- 767 Zhang, Y., Kong, D., Gan, R., Chiew, F.H.S., McVicar, T.R., Zhang, Q., Yang, Y., 2019. Coupled
768 estimation of 500 m and 8-day resolution global evapotranspiration and gross primary

769 production in 2002–2017. *Remote Sensing of Environment* 222, 165–182.
770 <https://doi.org/10.1016/j.rse.2018.12.031>
771 Zhao, W.L., Gentile, P., Reichstein, M., Zhang, Y., Zhou, S., Wen, Y., Lin, C., Li, X., Qiu, G.Y.,
772 2019. Physics-Constrained Machine Learning of Evapotranspiration. *Geophysical*
773 *Research Letters* 46, 14496–14507. <https://doi.org/10.1029/2019GL085291>
774 Zhou, S., Yu, B., Zhang, L., Huang, Y., Pan, M., Wang, G., 2016. A new method to partition
775 climate and catchment effect on the mean annual runoff based on the Budyko
776 complementary relationship: PARTITIONING THE CLIMATE AND CATCHMENT EFFECT ON
777 RUNOFF. *Water Resour. Res.* 52, 7163–7177. <https://doi.org/10.1002/2016WR019046>
778
779